Continuous Guided Strontium Beam with High Phase-Space Density

Chen, C.-C.; Bennetts, S.; González Escudero, R.; Pasquiou, B.; Schreck, F.

DOI
10.1103/PhysRevApplied.12.044014

Publication date
2019

Document Version
Final published version

Published in
Physical Review Applied

Continuous Guided Strontium Beam with High Phase-Space Density

Chun-Chia Chen (陳俊嘉),* Shayne Bennetts,† Rodrigo González Escudero, Benjamin Pasquiou, and Florian Schreck

Van der Waals-Zeeman Institute, Institute of Physics, University of Amsterdam, Science Park 904, 1098 XH Amsterdam, Netherlands

(Received 11 July 2019; revised manuscript received 23 August 2019; published 7 October 2019)

A continuous guided atomic beam of ^{88}Sr with a phase-space density exceeding 10^{-4} in the moving frame and a flux of 3×10^7 at. s^{-1} is demonstrated. This phase-space density is around 3 orders of magnitude higher than previously reported for steady-state atomic beams. We detail the architecture necessary to produce this ultracold-atom source and characterize its output after propagation for approximately 4 cm. With radial temperatures of less than 1 μK and a velocity of 8.4 cm s^{-1}, this source is ideal for a range of applications. For example, it could be used to replenish the gain medium of an active optical superradiant clock or be used to overcome the Dick effect, which can limit the performance of pulsed-mode atom interferometers, atomic clocks, and ultracold-atom-based sensors in general. Finally, this result represents a significant step toward the development of a steady-state atom laser.

DOI: 10.1103/PhysRevApplied.12.044014

I. INTRODUCTION

From atomic clocks [1] to atom interferometers [2], cold-atom and ultracold-atom devices are defining the state of the art of precision measurement. Cold-atom sensors are tackling fundamental questions such as detecting dark matter or dark energy [3–6], gravitational waves, [7–10] and variations of fundamental constants [11,12], as well as making precision measurements of physical constants [13–16]. In the applied domain, optical atomic clocks continue to set new records in timekeeping [17–19], while cold-atom gravimeters, gravity gradiometers, gyroscopes, and accelerometers are of growing importance for geology and navigation [20–23]. Yet almost all these cold-atom sensors and the atom sources they rely on operate in pulsed mode, which poses a fundamental limitation. The Dick effect [24,25], where frequency-noise aliasing arises from the dead time between sample interrogations, intrinsically limits the performance of a pulsed device.

Atomic clocks now reach sensitivities where the Dick effect limits performance [26,27]. Improvements in the optical clock local oscillator has allowed them to better preserve phase across the dead time [28,29]. Others synchronize multiple copies of the same apparatus to avoid dead time [22,30,31], or increase the duty cycle by performing multiple measurements after a single sample-preparation phase [32–34]. Hybridization of a cold-atom interferometer with other devices can combine the low offsets of atom interferometers with the higher bandwidth of classical devices in a single apparatus [23]. A fundamentally simpler approach would be to create a fully continuous device [35–38]. Active optical clocks [39,40] are a promising proposal for producing a new generation of optical clocks that are inherently continuous, circumventing both the Dick effect and other challenges now limiting optical lattice clocks, such as the thermal noise of the local oscillator. These are based on the principle of superradiant lasing of ultracold atoms inside a "bad" optical cavity. The operating principle has been demonstrated [41], even on strontium's optical clock transition [42], but what is desirable is a high-phase-space-density (PSD) continuous atom source to run the clock steady state [43,44]. Similarly, other cold-atom sensors would benefit from continuous operation, such as inertial sensors for navigation that could feature both absolute calibration and continuous measurement [45].

The development of atomic beams with high phase-space density has historically been closely tied to efforts to produce a steady-state atom laser [46], perhaps the ultimate source for many cold-atom sensors. Lahaye *et al.* [47,48] demonstrated steady-state beams with a PSD of 10^{-7} by repeatedly out-coupling rubidium atoms from a magneto-optical trap (MOT) and evaporatively cooling them as they traversed a 4.5-m-long magnetic waveguide. A chromium beam of 1×10^7 at. s^{-1} with a PSD of 3×10^{-8} was produced in the work reported in Refs. [49,50], and Knuffman *et al.* [51] produced a cesium beam of 5×10^{10} at. s^{-1} with a PSD of 4×10^{-8} for a focused-ion-beam source.

Here we present a continuous ^{88}Sr source delivering an atomic beam of 3×10^7 at. s^{-1} with a phase-space density of more than 10^{-4} in the moving frame. To

*beam@strontiumbec.com
†shayne.bennetts@uva.nl

enable an extremely low forward velocity of approximately 10 cm s^{-1}, this beam is supported against gravity by an optical dipole guide. This source could feed an atom interferometer in continuous-operation mode, in particular using the $^1S_0$-$^3P_0$ clock transition in a magic wavelength guide [52,53]. Moreover, this high-PSD atomic beam could provide the gain medium for a steady-state superradiant laser [39,40,42], and produce a clock laser with linewidth substantially narrower than the transition linewidth [54]. Lastly, this beam could possibly be the source for a continuous atom laser [55–58].

This paper is structured as follows. Section II describes the experimental setup and the various steps and methods necessary to produce the beam. In Sec. III, we discuss figures of merit for characterizing cold atomic beams. We then present our measurement protocols and the results we obtain for two strontium isotopes in Sec. IV. Lastly, in Sec. V we discuss possible applications for our continuous high-phase-space-density atomic beam and summarize our results.

II. EXPERIMENT

Our approach to producing a continuous, cold, bright atomic beam is based on flowing gaseous strontium through a series of spatially distributed laser cooling and guiding stages. Our scheme is illustrated in Fig. 1. The first stages are responsible for cooling atoms, beginning with an approximately–800-K oven and finishing with an approximately-10-μK steady-state MOT. We have previously reported on this MOT architecture [59]. We next outcouple atoms from the MOT into an optical dipole guide, creating a bright, slow atomic beam. Transverse cooling of this atomic beam together with measures to detune MOT light and prevent it from interacting with the beam are critical to achieve high performance. We characterize the resulting atomic beam at a location approximately 37 mm from the MOT. In the following section, we explain the details of this apparatus.

A. Steady-state MOT atom source

Beginning from an 800-K hot oven, atoms are transversely cooled, Zeeman slowed, and captured by a two-dimensional continuous MOT with "push" beams, all operated on the 30-MHz-linewidth $^1S_0$-$^1P_1$ transition. This first stage creates a beam with a flux of 2.7×10^9 ^{88}Sr atoms per second at approximately 10 mK with a vertical downward velocity of a few meters per second. This beam is transversely cooled by a molasses operating on the 7.4-kHz-linewidth $^1S_0$-$^3P_1$ transition, reducing the radial temperature to approximately 10 μK and allowing the beam to efficiently propagate to a second, lower chamber through a baffle. The baffle and the dual chamber designs are used to prevent ultracold atoms in the lower chamber from being heated by the continuously operating cooling

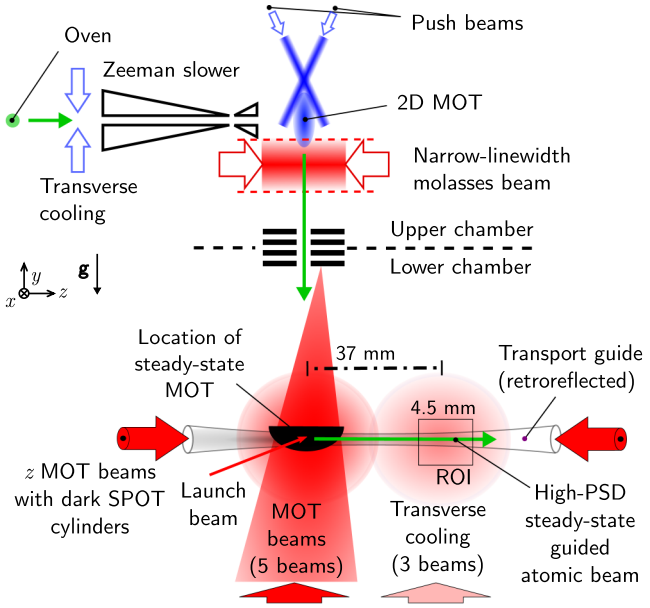

FIG. 1. Production of a high-PSD atomic beam. An oven emits strontium atoms that are transversely cooled and slowed by a Zeeman slower, the output from which is caught by a two-dimensional (2D) MOT, all operating on the $^1S_0$-$^1P_1$ transition (beams in blue). The $^1S_0$-$^3P_1$ transition (beams in red) is then used to radially cool the atoms by an optical molasses, before they fall under gravity to a baffled second chamber. Here atoms are recaptured in a steady-state five-beam MOT, again operated on the $^1S_0$-$^3P_1$ transition. The MOT is overlapped with an optical guide, into which atoms are launched with a mean velocity of approximately 10 cm s^{-1}. This guided beam is radially cooled along the way by three low-intensity molasses beams. The ROI where we characterize the atomic beam is located 37 mm from the MOT.

light in the upper chamber. This can be critical depending on the time spent by the atoms in the lower chamber.

The falling atomic beam is captured by a steady-state three-dimensional MOT operating on the 7.4-kHz $^1S_0$-$^3P_1$ transition. The MOT geometry consists of five beams in an orthogonal configuration. In the vertical direction, we shine a single MOT beam from below and rely on gravity to provide the downward restoring force. The MOT quadrupole magnetic field has gradients of 0.55, -0.32, and -0.23 G cm^{-1} in the x, y, and z directions, respectively. Atoms in the MOT typically have a temperature ranging from 5 to 30 μK. The MOT laser detunings and intensities are adjusted to maximize the performance of the atomic beam in the region of interest (ROI; see Fig. 1) rather than the MOT itself.

To address atoms with Doppler shifts much larger than the 7.4-kHz atomic linewidth, we use acousto-optic modulators to frequency broaden the MOT beams to a comblike structure with a spacing of $\delta \sim 20$ kHz (corresponding to $2\text{–}3 \times \Gamma_{^1S_0\text{-}^3P_1}/2\pi$). The detuning ranges $(\Delta_1; \delta; \Delta_2)$ are $(-2.2; 0.015; -0.66)$, $(-5.2; 0.02; -0.95)$,

and $(-2.2; 0.016; -0.82)$ MHz for the x, y, and z axis, respectively. The power in each x-axis, y-axis, and z-axis MOT beam is 1.2, 10.8, and 1.14 mW and the $1/e^2$ beam diameter is 47, 68, and 48 mm, respectively. The single beam in the y direction is focused 22 cm above the center of the MOT quadrupole magnetic field and its $1/e^2$ diameter is approximately 35 mm at the MOT location.

The MOT beams along the z axis provide confinement that can prevent the emission of an atomic beam along the z direction. To mitigate this problem, we bore an 8-mm-diameter hole in the center of the two mirrors directing the z MOT beams from each side of the vacuum chamber (see Fig. 1). This allows the insertion of an extra pair of low-intensity MOT beams down the z axis of the MOT, strong enough to trap the cold MOT atoms but weak compared with the other MOT beams, which are optimized to capture hot incoming atoms. These additional beams fill up the holes entirely with a $1/e^2$ diameter of approximately 8 mm, and they have a smaller detuning range of $(-1.25; 0.017; -0.85)$ MHz and a much lower power of 5 μW. In addition to facilitating the out-coupling of a guided atomic beam, the resulting MOT cloud is also elongated along the z axis, resulting in greater spatial overlap with the guide. Further details describing the steady-state three-dimensional MOT can be found in Ref. [59].

B. Transport guide

We continuously load atoms from the steady-state MOT into a "transport" guide, formed by an optical dipole beam overlapped with the MOT cloud and propagating along the z axis. The guide is produced by focusing 12 W from a 1070-nm ytterbium fiber laser (IPG YLR-20-LP with a linewidth of 1.1 nm) to a 92-μm $1/e^2$ radius waist at the location of the MOT. To extend the guide length and increase the uniformity of the guide potential depth we retroreflect the (incoherent) beam, focusing its second pass approximately 35 mm from the MOT along the z axis in the direction of the atomic beam propagation, with the same waist as in the first pass. The 35-mm distance between foci is chosen to be on the same order as the Rayleigh length (25 mm) of both of these beams. By adapting the power of the retroreflected beam with a polarizing beam splitter and a $\lambda/2$ waveplate, we can tune and flatten the potential landscape along the guide. The effective trap depth at the MOT location is approximately 35–40 μK, and 37 mm away, where the potential is flattened the depth is approximately 25 μK and the radial trapping frequency $\omega_r = 2\pi \times 185$ Hz. This deep, large-volume trap at the MOT location increases the loading efficiency, and the flat potential for the final beam helps with further laser cooling stages by reducing light-shift variations. The off-resonant scattering rate in the guide is negligible at approximately 0.1 Hz.

C. Dark spontaneous-force-optical-trap cylinder

In our implementation, two MOT beams are overlapped and collinear with the transport guide in the z direction. It typically takes approximately 0.4 s for atoms in the atomic beam to propagate the 37 mm from the MOT to the characterization location. Over such a long interaction time even a very small amount of resonant MOT light would be sufficient for the MOT restoring force to return atoms from the atomic beam to the MOT, thus devastating the beam's flux and temperature. Two factors mitigate this effect. Firstly, the MOT-light intensity is much lower in the 8-mm-core beam. Secondly, the $^3P_1$ $m_J = -1$ state experiences a 0.48 MHz cm^{-1} Zeeman shift due to the MOT's quadrupole magnetic field, quickly shifting the atoms propagating in the beam out of resonance with the MOT light. However, these measures alone are not sufficient.

To further reduce the interaction between the MOT beams and the atomic beam, we adapt the dark spontaneous-force-optical-trap (SPOT) technique [60]. Along both MOT beams in the z direction, we image a 20 cm-long, 600-μm-outer-diameter cylinder. By overlapping this shadow with the transport guide, we further darken the MOT region extending far beyond the characterization location 37 mm from the MOT. The cylinder is assembled by our suspending a stainless-steel capillary within each inner z-axis MOT beam. The capillary has an inner diameter of 400 μm, through which three 50-μm-diameter twisted wires pass. At the ends of each cylinder, the three thin wires are pulled taut triangularly sideways, forming a tetrahedron shape, and are glued to an x-y translator (Thorlabs, CXY1, 30-mm cage x-y translator); see Figs. 2(a) and 2(b). The x-y translators are used to precisely position each cylinder within a MOT beam. In front of each collimated MOT beam, we use a simple two-lens system in the f -$2f$ -f configuration ($f = 500$ mm) to image the cylinder's shadow onto the transport guide with a magnification of 1.

We characterize the performance of these dark SPOT cylinders by imaging the shadow actually produced on the atoms, by collecting leakage light transmitted through MOT mirrors and imaging it onto a camera. By varying the image plane on the camera chip, we can select a specific object plane along the transport guide, as shown in the example in Fig. 2(c). Using this method, we check the alignment of the dark volume across the atom's whole 37-mm traveling distance. We measure an attenuation of the MOT light by a factor of approximately 30–40 along the center of the transport guide due to the dark SPOT cylinders. The darkness is ultimately limited by imperfections in the cylinder's surface and imaging, and by Poisson's spot from diffraction. Another MOT-beam geometry, without a beam in the z direction, could be envisioned, but some sort of dark slit would still be required to darken the region where the guide crosses out of the MOT beam.

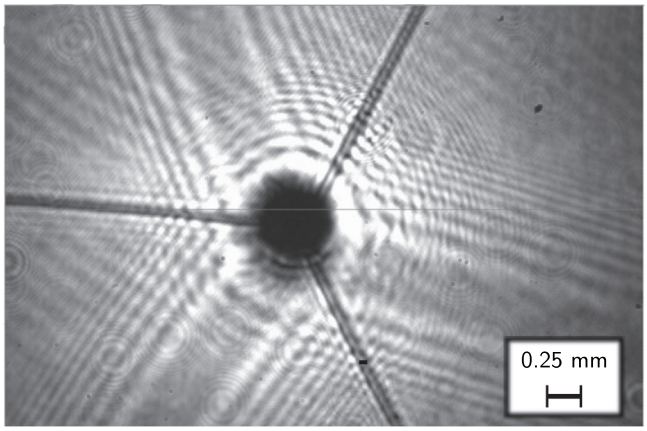

FIG. 2. MOT-beam shadow-casting structure. To protect the guided atomic beam from the copropagating MOT light, two cylinders are imaged at the guide location, one for each MOT beam along the z axis. This structure consists of a capillary suspended with the use of three threaded 50-μm-diameter wires. The picture shows the MOT-light attenuation due to one cylinder, imaged at the plane corresponding to one end of a single cylinder. A dark cylinder achieves an attenuation of approximately 30–40 throughout its imaged length. The lines toward the edges are from the imaged suspension wires.

D. Launch beam

With both the reduced MOT-beam intensities along the z axis and the effect of the dark SPOT cylinders, we observe out-coupling of atoms into the transport guide, followed by propagation across 37 mm. However, the atoms' speed is extremely low, dictated mainly by the MOT temperature, and is beyond the experimentalist's control. The resulting flux varies strongly, and any imperfection in the engineered darkness results in a beam that appears to stop at seemingly random places. Moreover, low propagation speeds render the beam more vulnerable to losses such as background-gas collisions and off-resonant scattering from the transport guide. To remedy this situation, we add a "launch" laser beam resonant with the $^1S_0$-$^3P_1$ π transition. This 250-μm-waist beam shines 30 nW of light at the overlap between the MOT and the transport guide, forming an angle with the guide of 6° (see Fig. 1). With the help of this launch beam, we can out-couple MOT atoms into the guide with a well-controlled mean velocity ranging from 8 to 25 cm s^{-1} (see Sec. IV). During the remainder of this work, we typically use a launch-beam intensity corresponding to a measured velocity of 8–9 cm s^{-1}.

E. Transverse cooling

By applying transverse cooling with the $^1S_0$-$^3P_1$ π transition to atoms propagating along the guide, we can both minimize the atomic beam's transverse temperature and optimize flux by removing evaporative losses. To this end, we place three single-frequency laser beams with propagation axes perpendicular to the atomic beam, a 36 mm $1/e^2$ diameter beam propagating upward along the y axis, and a counterpropagating 28.8 mm $1/e^2$ diameter beam pair along the x axis, as shown in Fig. 1. These beams are centered approximately 35 mm from the MOT center and have powers of 1.4 and 6.75 μW for the horizontal and vertical axes, respectively. This gives a peak combined intensity of approximately 0.5 times the saturation parameter. These transverse cooling beams have a frequency 80 kHz blue detuned from the $^1S_0$-$^3P_1$ π transition for free atoms. As a result of the differential light shift from the guide, this corresponds to an approximately-200-kHz red detuning for atoms passing along the center of the guide. With this transverse cooling, the radial temperature is ultimately lowered to about 1 μK and the flux is increased by a factor of approximately 2.

III. FIGURES OF MERIT: AN OVERVIEW

In the literature a variety of measures have been used to characterize the performance of atomic beams, with each measure optimized for different applications. In this section we introduce and summarize these figures of merit as well as put them into context for applications such as interferometry, gain media for superradiant lasers, and atom lasers.

Assuming a Gaussian density distribution of the atoms in the radial direction, the beam flux Φ can be represented by

$$\begin{aligned}\Phi &= \int_0^\infty n_0 \exp\left(-\frac{r^2}{2\Delta r^2}\right) 2\pi r dr\, \bar{v}_z \\ &= 2\pi\,\Delta r^2\, n_0 \bar{v}_z = \rho_L \bar{v}_z,\end{aligned} \tag{1}$$

where Δr is the root-mean-square one-dimensional (1D) spatial spread, n_0 is the peak density, ρ_L is the linear density, and $\bar{v}_z$ is the mean longitudinal velocity. All these parameters can be directly measured in our experiment. The flux density is the flux per unit cross-section area, given by $\rho_\Phi = \Phi/\pi\,\Delta r^2$.

We also give the beam performance in terms of the gas phase-space density, usually used for ultracold and quantum degenerate gases. The PSD is expressed in the moving frame as

$$\begin{aligned}\rho_{\mathrm{PSD}} &= n_0\, \lambda_{\mathrm{dB},r}^2\, \lambda_{\mathrm{dB},z} \\ &= n_0 \left(\frac{h}{\sqrt{2\pi\, m k_B T_r}}\right)^2 \frac{h}{\sqrt{2\pi\, m k_B T_z}},\end{aligned} \tag{2}$$

where h is the Planck constant, k_B is the Boltzmann constant, m is the atomic mass, and $\lambda_{\mathrm{dB},r}$ ($\lambda_{\mathrm{dB},z}$) is the thermal de Broglie wavelength associated with the 1D temperature T_r(T_z) in the radial (axial) direction. Since we observe that

the velocities follow Gaussian distributions, these effective 1D temperatures are directly related to the measured root-mean-square 1D velocity spreads by the relations $\Delta v_r = \sqrt{k_B T_r/m}$ and $\Delta v_z = \sqrt{k_B T_z/m}$.

There are two ways in which we estimate the peak atom number density n_0. Firstly, we can use absorption imaging and fit a Gaussian profile to estimate the peak density. Alternatively, we may assume that the atom density inside the guide follows a Boltzmann distribution with radial temperature T_r. The density distribution then follows $n(r) = n_{0,\mathrm{therm}} \exp[-(U(r)/k_B T_r)]$, where $U(r)$ is the potential energy due to the transport guide. This is valid in the case of a gas in thermal equilibrium because of a high collision rate. For a guide that is deep compared with the radial temperature, its radial potential can be approximated by a harmonic oscillator potential with trapping frequency $\omega_r/2\pi$. With Eq. (1), the peak density in the thermalized case is then related to the linear density by $\rho_L = n_{0,\mathrm{therm}}\, 2\pi k_B T_r/m\omega_r^2$, and the expression for the phase-space density in Eq. (2) can be written as

$$\begin{aligned}\rho_{\mathrm{PSD,therm}} &= n_{0,\mathrm{therm}}\, \lambda_{\mathrm{dB},r}^2\, \lambda_{\mathrm{dB},z} \\ &= \rho_L \left(\frac{h\omega_r}{2\pi\, k_B T_r}\right)^2 \frac{h}{\sqrt{2\pi\, m k_B T_z}}.\end{aligned} \tag{3}$$

The temperatures T_r and T_z, the trapping frequency $\omega_r/2\pi$, and the linear density ρ_L are directly accessible from the experimental data.

Another quantity of interest for establishing the usefulness of a beam source is its brightness (or radiance). In the literature it is often expressed by the flux density divided by the solid angle Ω of the beam divergence, and it is of primary interest to characterize ion beams [61]. Since our beam is strongly confined by the transport guide and since the axial speed is very low, the beam divergence can be negligible between, for example, two regions of interrogation in an interferometry scheme. The brightness is thus not the most-suitable quantity to characterize our beam. We nonetheless provide it for completeness in the case of a cold atomic beam [62,63]:

$$\mathcal{R} = \frac{\Phi}{\pi\, \Delta r^2\, \Omega}, \tag{4}$$

where $\Omega = \pi(\Delta v_r/\bar{v}_z)^2$. Similarly, the brilliance $\mathcal{B}$ of the beam is given by

$$\mathcal{B} = \mathcal{R}\frac{\bar{v}_z}{\Delta v_z} = \frac{\Phi\, \bar{v}_z^3}{\pi^2 \Delta r^2\, \Delta v_z \Delta v_r^2}. \tag{5}$$

Since our beam is guided, a better-suited figure of merit is the velocity brightness $\mathcal{R}_v$, expressed as the flux per unit beam area per three-dimensional velocity spread:

$$\mathcal{R}_v = \frac{\Phi}{\pi\, \Delta r^2\, \Delta v_z \Delta v_r^2}. \tag{6}$$

This expression is commonly used to characterize atomic beams for interferometry-based precision measurement [64–67] and to characterize atom lasers [46,68,69].

IV. RESULTS

We now present the results obtained from characterizing the atomic beam at a location 37 mm from the MOT center, in a region out of the MOT laser beam and out of resonance with scattered light from these beams. We measure the axial mean velocity and velocity spread, and the radial velocity spread. We also measure the density, linear density, and transverse spatial spread. From these we infer the beam flux, phase-space density, and brightness. All these quantities are summarized in Table I.

A. Axial velocity and velocity spread

Owing to the extremely low temperatures reached in a strontium MOT operated on the narrow $^1S_0$-$^3P_1$ line, the resulting atomic beam can be extremely slow. This often-welcome feature prevents us from characterizing the beam velocity and velocity spread by the conventional method of Doppler-sensitive laser-induced fluorescence [70]. To have a laser-induced-fluorescence signal with sufficient velocity resolution, the Doppler shift has to be large compared with the transition linewidth of the fluorescent light. The velocity of our atomic beam is on the order of 10 cm s^{-1}, corresponding to a Doppler shift of only 217 kHz for the 30-MHz-wide $^1S_0$-$^1P_1$ transition, clearly an insufficient resolution. Alternatively, the weak 7.4-kHz-wide $^1S_0$-$^3P_1$ transition would give a shift of 145 kHz but insufficient fluorescence signal due to the low scattering rate.

To measure the axial atomic beam velocity and velocity spread, we instead apply a 1-ms pulse of light resonant with the $^1S_0$-$^1P_1$ transition, with a horizontal beam perpendicular to the guided atomic beam. This pulse ejects a packet of atoms from the guide; see Fig. 3(a). We assume that spontaneously emitted photons are equally distributed in all directions during the ejection process, so the z-axis mean velocity is not affected. We infer the mean velocity $\bar{v}_z$ and velocity spread Δv_z by examining the evolution of the atom packet propagating alongside the transport guide. We perform this characterization for atoms in the transport guide located 37 mm from the MOT, within the approximately-4-mm-long ROI of our imaging setup. As a result of the architecture of our tunable transport guide (see Sec. II), the potential landscape along the guide axis is essentially flat across the ROI. We therefore assume the beam velocity to be constant throughout the ROI. We measure the velocity for several launch-beam intensities, and

TABLE I. Characteristics of the beam, for both ^{88}Sr and ^{84}Sr, measured 37 mm away from the MOT. The symbols and their expressions are detailed in the main text. All uncertainties are taken as the standard deviation from the fitted data. $\bar{v}_z$ and Δv_z could not be measured for ^{84}Sr as the flux is not large enough, so we assume the same values as for ^{88}Sr, scaled by the mass ratio.

Parameter	^{88}Sr beam	^{84}Sr beam
Axial temperature T_z (μK)	29(2)	29(2)
Radial temperature T_r (μK)	0.89(4)	2.0(1)
Axial velocity $\bar{v}_z$ (cm s^{-1})	8.4(4)	8.8(4)
Axial velocity spread Δv_z (cm s^{-1})	5.2(2)	5.3(2)
Radial velocity spread Δv_r (cm s^{-1})	0.92(2)	1.41(4)
Spatial spread Δr (μm)	23.3(4)	19.7(1.0)
Linear density ρ_L (at. m^{-1})	$3.88(8) \times 10^{8}$	$1.04(5) \times 10^{7}$
Peak density n_0 (at. m^{-3})	$1.14(4) \times 10^{17}$	$4.2(5) \times 10^{15}$
Flux Φ (at. s^{-1})	$3.25(14) \times 10^{7}$	$9.1(6) \times 10^{5}$
Flux density ρ_Φ (at. s^{-1} m^{-2})	$1.02(5) \times 10^{20}$	$2.9(4) \times 10^{17}$
Radial trapping frequency $\omega_r/2\pi$ (Hz)	185(10)	185(10)
Collision rate $\Gamma_{\rm el}$ (s^{-1})	$3.5(2) \times 10^{-4}$	0.11(2)
PSD $\rho_{\rm PSD}$	$1.5(2) \times 10^{-4}$	$2.7(4) \times 10^{-6}$
Alternative PSD $\rho_{\rm PSD,therm}$	$1.3(2) \times 10^{-3}$	$7.1(1.2) \times 10^{-6}$
Brightness $\mathcal{R}$ (at. s^{-1} m^{-2} sr^{-1})	$5.0(7) \times 10^{17}$	$9(2) \times 10^{15}$
Brilliance $\mathcal{B}$ (at. s^{-1} m^{-2} sr^{-1})	$2.5(5) \times 10^{18}$	$5(1) \times 10^{16}$
Velocity brightness $\mathcal{R}_v$ (at. s^{2} m^{-5})	$4.3(4) \times 10^{21}$	$7(1) \times 10^{19}$

confirm that we can adjust the mean velocity within the range from 8 to 25 cm s^{-1} [see Fig. 3(b)]. We observe that for all launch-beam intensities the atomic beam has a similar axial velocity spread of 5.2(2) cm s^{-1} [see Fig. 3(c)]. This velocity spread corresponds to a 1D axial temperature of 29(2) μK. By looking at the momentum imparted to the atomic packet by the ejection pulse in the radial direction, we check that the heating due to this pulse is negligible compared with the measured axial temperature.

B. Radial velocity spread

We measure the radial velocity spread in a more-conventional way, by switching off the transport guide and measuring the atomic beam size after ballistic expansion [see Fig. 4(a)]. We obtain a radial temperature of 1.93(5) μK averaged over the entire ROI. With the addition of transverse cooling light (see Sec. II), the flux increases by a factor of approximately 2 and the radial temperature reduces to 0.89(4) μK, corresponding to a radial velocity spread of 0.92(2) cm s^{-1} [see Fig. 4(b)].

Within the ROI, we observe a mild variation of both the density and the radial velocity spread along the transport-guide axis. More precisely, as the atoms propagate, both the flux and the radial temperature reduce. Without transverse cooling light, this can be explained by radial losses, which could be enhanced by eventual corrugations of the guide potential that transfer momentum from the axial direction to the radial direction. When the transverse cooling light is applied, the radial temperature slowly decreases, as expected, with the atoms' travel time. The losses are thus strongly reduced, leading to a slower decrease of the flux.

C. Density, flux, and brightness

Our imaging system resolution of 4.5 μm is sufficient to image the beam density profile by absorption imaging (with a negligible time of flight of 0.1 ms) while staying within the dynamic range of the camera. The linear density ρ_L can be estimated by integrating the atom number over the radial direction and along the full length of the ROI. We fit the beam averaged along the propagation axis to the Gaussian profile in Eq. (1) in order to estimate the peak density n_0 and the spatial spread Δr. From all the measured quantities and the expressions given in Sec. III, we extract the results summarized in Table I for the ^{88}Sr and ^{84}Sr isotopes. From the measured flux captured by the MOT and the flux observed at the end of the guide, we estimate the transfer efficiency from the MOT to the beam to be approximately 30%.

D. Thermalization

As shown in Table I, there is a clear discrepancy between the $\rho_{\rm PSD}$ and $\rho_{\rm PSD,therm}$ values, with the latter being higher by a factor of approximately 10 for ^{88}Sr and approximately 3 for ^{84}Sr. The expression for $\rho_{\rm PSD}$ estimates the density on the basis of the measured atomic beam radius rather than assuming a Boltzmann distribution in a harmonic trap. We can therefore understand this discrepancy to be due to the absence of thermalization, which can be seen from the differences between the axial and radial temperatures. Without a thermalized sample, $\rho_{\rm PSD,therm}$ is not reliable, so we use the smaller value for the PSD given by $\rho_{\rm PSD}$.

Following the work reported in Ref. [71], we can estimate the elastic collision rate within the beam. From

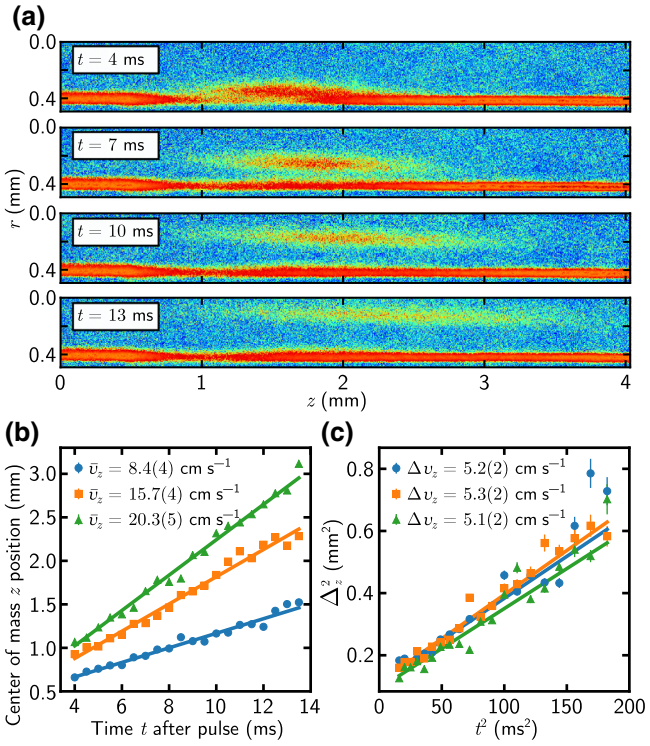

FIG. 3. Axial velocity and velocity spread of the atomic beam. (a) Steady-state atomic beam after the application of a 1-ms pulse of light resonant with the $^1S_0$-$^1P_1$ transition. The ejected wavepacket is in free flight along z for time t, after which an absorption image is taken. (b) Center-of-mass position and (c) width Δz of the ejected wavepacket for three different intensities of the launch beam (see Sec. II). The lines are linear fits, from which we extract (b) the axial velocity $\bar{v}_z$ and (c) the velocity spread Δv_z. Error bars on data points in (b),(c) show the standard deviation from Gaussian fits of the ejected wavepacket.

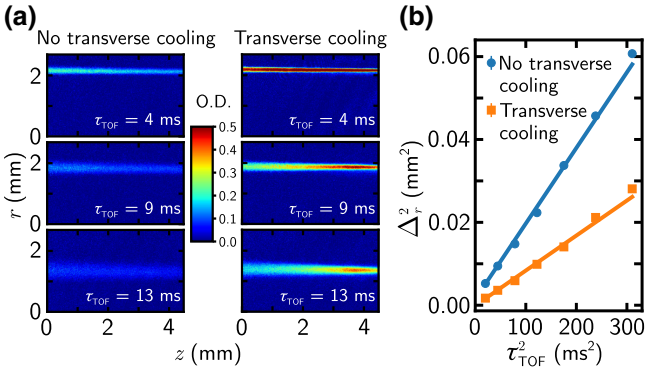

FIG. 4. Effect of transverse cooling on the beam radial velocity spread. (a) Absorption images of the steady-state atomic beam, taken after switching the transport guide and laser cooling beams *off* and letting the cloud expand for various times of flight τ_{TOF}. The beam is shown both without (left) and with (right) transverse cooling applied (see Sec. II). For clarity, we set the maximum optical density to 0.5 on the color scale, which means that some pictures are saturated. (b) Expansion of the beam size Δ_r in free flight, from which we extract the radial velocity spread. The lines are linear fits, giving $\Delta v_r = 1.36(2)$ cm s^{-1} without transverse cooling and $\Delta v_r = 0.92(2)$ cm s^{-1} with transverse cooling. This corresponds to radial temperature $T_r = 1.93(5)$ μK and $T_r = 0.89(4)$ μK, respectively. The small error bars in (b) give the standard deviation from Gaussian fits of density profiles integrated along the whole ROI.

our measurements of the anisotropic density and velocity distributions, we can estimate the elastic collision rates to be $\Gamma_{\mathrm{el},^{88}\mathrm{Sr}} = 3.5(2) \times 10^{-4}$ s^{-1} and $\Gamma_{\mathrm{el},^{84}\mathrm{Sr}} = 0.11(2)$ s^{-1}. Given the propagation time from the MOT of less than 0.5 s, the scattering rates for both isotopes are insufficient to thermalize the atoms.

Despite the much higher density, the collision rate for ^{88}Sr is approximately 300 times smaller than for ^{84}Sr, due to the scattering length $a_{\mathrm{scat},^{88}\mathrm{Sr}} = -1.4\ a_0$ being much smaller than $a_{\mathrm{scat},^{84}\mathrm{Sr}} = 122.7\ a_0$, where a_0 is the Bohr radius. These rates can be expressed as $\Gamma_{\mathrm{el}} = n_0 \sigma_{\mathrm{cross}} v_{\mathrm{coll}}$, where $\sigma_{\mathrm{cross}} = 8\pi a_{\mathrm{scat}}^2$ is the elastic cross section and $v_{\mathrm{coll}} = \sqrt{2k_B T_{\mathrm{eff}}/\pi m}$ is the mean relative velocity, for an effective isotropic temperature $T_{\mathrm{eff},^{88}\mathrm{Sr}} \sim 8\ \mu$K and $T_{\mathrm{eff},^{84}\mathrm{Sr}} \sim 10\ \mu$K.

V. DISCUSSION

There are three essential elements that enable the performance demonstrated by our steady-state beam. First, our architecture [59] spatially separates regions requiring laser cooling on the 30-MHz-linewidth $^1S_0$-$^1P_1$ transition from regions using laser cooling on the 7.4-kHz-linewidth $^1S_0$-$^3P_1$ transition. This spatial separation allows us to simultaneously combine the strengths of both transitions: slowing fast atoms from an oven to a few meters per second, then cooling them further to demonstrate a continuous atomic beam with extremely low velocity (approximately 10 cm s^{-1}) and velocity spread. Second, we carefully engineer the $^1S_0$-$^3P_1$ laser-cooling light intensity and frequency in order to decouple the atoms inside the beam from harmful photons. This is achieved by using the dark SPOT cylinders, and by selecting the frequency ranges and geometry of the various MOT beams (in particular the two MOT beam pairs copropagating along the z axis using hollowed-out mirrors). Third, we radially cool atoms as they propagate inside the transport guide, using the nonmagnetic $^1S_0$-$^3P_1$ transition. In this way we increase the beam flux and reduce its radial velocity spread in the region of interest.

The beam thus produced is stable over time, and the setup described has been operated (although not continuously) for months without the need for any major changes or beam realignments. The main contribution to long-term performance drifts is from variations in the background magnetic field. These can significantly affect the positioning of the MOT due to the very low magnetic field gradients used (approximately 0.3 G cm^{-1}). When

required, we compensate these drifts using three magnetic coil pairs producing uniform offset fields along each axis. The most-sensitive component in the setup is the alignment of the dark SPOT cylinders. This is due to the significant force that resonant scattering from residual MOT light can impart on the extremely slow atoms propagating within the guide. However, once the cylinders have been aligned, the beam performance remains stable.

The steady-state beam we demonstrate here has a phase-space density around 3 orders of magnitude higher than any previous steady-state atomic beam. The velocity brightness $\mathcal{R}_v = 4.3(4) \times 10^{21}$ for ^{88}Sr is approaching what has been reached by pulsed quasi-cw atom lasers [46,69]; for example, $\mathcal{R}_v = 2 \times 10^{24}$ in Ref. [68].

An immediate application for such a system might be continuously replenishing the gain medium of a steady-state superradiant active clock. There has been significant interest in the development of active optical clocks in recent years [39,40]. There have been pulsed demonstrations on the strontium clock transition [42] and a great deal of theoretical work [54,72–76], but any active clock requires replenishment of the atoms used for the gain medium. For the $^1S_0$-$^3P_0$ clock transition, modeling suggests that an ideal atomic source would consist of a guided continuous beam with a flux of more than 1×10^7 ^{88}Sr atoms per second and a velocity of approximately 10 cm s^{-1}, criteria fulfilled by the beam we have demonstrated.

Another interesting application is steady-state interferometry schemes that aim to operate in a continuous mode, eliminating the Dick effect. This might be particularly important for long interrogation times, for example, making use of the $^1S_0$-$^3P_0$ transition [52,53], which has been proposed for gravitational-wave detectors [9], although most likely an additional cooling stage is necessary for interferometry applications.

While the low axial velocity is ideal for some applications, it reduces the brightness and brilliance figures of merit typically used for applications such as milling with ion beams. This, along with the reduced flux compared with other systems [61], would likely limit direct use in applications such as high-current ion-beam sources or high-rate doping. However, it can be a good starting point for ion-beam sources where the goal is to achieve the highest resolution. Similarly, this continuous, low-spread beam is a good source for high-repetition-rate deterministic single-ion sources [77,78].

For many applications the ultimate atomic beam source would be a steady-state continuous atom laser, and efforts toward this goal produced the highest phase-space-density beams reported [47,48]. The work here represents a major step toward this goal even though it is preliminary in many aspects. A better control of the axial beam velocity is possible in several ways, one of which was recently demonstrated in our group [79]. By reducing the velocity and increasing the density, it might be possible with the ^{84}Sr isotope to increase the elastic collision rate $\Gamma_{\rm el}$ and reach a regime where collisions dominate [47,58]. This would enable evaporative cooling along the dipole guide [48,57,80], which would increase the beam PSD and hopefully produce a continuous atom laser [46,68].

To summarize, we demonstrate a continuous guided atomic beam of ^{88}Sr with a phase-space density more than 3 orders of magnitude higher than in previously reported systems. Our beam has an extremely low mean velocity $\bar{v}_z = 8.4(4)$ cm s^{-1}, radial spatial spread $\Delta r = 23.3(4)$ μm, and radial velocity spread $\Delta v_r = 0.92(2)$ cm s^{-1}. This corresponds to a radial temperature of just 0.89(4) μK. The beam flux $\Phi = 3.25(14) \times 10^7$ at. s^{-1}, and it reaches a PSD of $\rho_{\rm PSD} = 1.5(2) \times 10^{-4}$. Using the ^{84}Sr isotope (abundance 0.56%), we obtain a reduced phase-space density, but the longer scattering length means that our beam is approaching the collisionally dense regime, where evaporative cooling can be used to rapidly increase phase-space density. This represents a significant step toward the demonstration of a steady-state atom laser. Moreover, this beam is likely to find immediate application in efforts to demonstrate a steady-state superradiant active optical clock. A beam with such output performance could fulfill the demands of other applications requiring both ultracold atoms and uninterrupted operation, such as continuous atom interferometers, clocks, ion sources, and steady-state atom lasers.

ACKNOWLEDGMENTS

We thank Andrea Bertoldi for careful reading of the manuscript and providing insightful comments. We thank the Dutch Research Council (NWO) for funding through Vici Grant No. 680-47-619 and the European Research Council for funding under Project No. 615117 (QuantStro). This project received funding from the European Union's Horizon 2020 research and innovation program under Grant Agreement No. 820404 (iqClock project). B.P. thanks the NWO for funding through Veni Grant No. 680-47-438. C.-C.C. thanks the Ministry of Education of the Republic of China (Taiwan) for a Ministry of Education Technologies Incubation Scholarship.

[1] Andrew D. Ludlow, Martin M. Boyd, Jun Ye, E. Peik, and P. O. Schmidt, Optical atomic clocks, Rev. Mod. Phys. **87**, 637 (2015).

[2] Alexander D. Cronin, Jörg Schmiedmayer, and David E. Pritchard, Optics and interferometry with atoms and molecules, Rev. Mod. Phys. **81**, 1051 (2009).

[3] P. Wcisło *et al.*, New bounds on dark matter coupling from a global network of optical atomic clocks, Sci. Adv. **4**, eaau4869 (2018).

[4] A. Hees, J. Guéna, M. Abgrall, S. Bize, and P. Wolf, Searching for an Oscillating Massive Scalar Field as a Dark Matter Candidate Using Atomic Hyperfine Frequency Comparisons, Phys. Rev. Lett. **117**, 061301 (2016).

[5] Andrew A. Geraci and Andrei Derevianko, Sensitivity of Atom Interferometry to Ultralight Scalar Field Dark Matter, Phys. Rev. Lett. **117**, 261301 (2016).

[6] Matt Jaffe, Philipp Haslinger, Victoria Xu, Paul Hamilton, Amol Upadhye, Benjamin Elder, Justin Khoury, and Holger Müller, Testing sub-gravitational forces on atoms from a miniature in-vacuum source mass, Nat. Phys. **13**, 938 (2017).

[7] B. Canuel *et al.*, Exploring gravity with the MIGA large scale atom interferometer, Sci. Rep. **8**, 14064 (2018).

[8] Peter W. Graham, Jason M. Hogan, Mark A. Kasevich, and Surjeet Rajendran, New Method for Gravitational Wave Detection with Atomic Sensors, Phys. Rev. Lett. **110**, 171102 (2013).

[9] Jason M. Hogan, David M. S. Johnson, Susannah Dickerson, Tim Kovachy, Alex Sugarbaker, Sheng-Wey Chiow, Peter W. Graham, Mark A. Kasevich, Babak Saif, Surjeet Rajendran, Philippe Bouyer, Bernard D. Seery, Lee Feinberg, and Ritva Keski-Kuha, An atomic gravitational wave interferometric sensor in low earth orbit (AGIS-LEO), Gen. Rel. Gravit. **43**, 1953 (2011).

[10] S. Kolkowitz, I. Pikovski, N. Langellier, M. D. Lukin, R. L. Walsworth, and J. Ye, Gravitational wave detection with optical lattice atomic clocks, Phys. Rev. D **94**, 124043 (2016).

[11] C. J. A. P. Martins, The status of varying constants: A review of the physics, searches and implications, Rep. Prog. Phys. **80**, 126902 (2017).

[12] R. M. Godun, P. B. R. Nisbet-Jones, J. M. Jones, S. A. King, L. A. M. Johnson, H. S. Margolis, K. Szymaniec, S. N. Lea, K. Bongs, and P. Gill, Frequency Ratio of two Optical Clock Transitions in $^{171}Yb^{+}$ and Constraints on the Time Variation of Fundamental Constants, Phys. Rev. Lett. **113**, 210801 (2014).

[13] Richard H. Parker, Chenghui Yu, Weicheng Zhong, Brian Estey, and Holger Müller, Measurement of the fine-structure constant as a test of the standard model, Science **360**, 191 (2018).

[14] A. Bertoldi, G. Lamporesi, L. Cacciapuoti, M. de Angelis, M. Fattori, T. Petelski, A. Peters, M. Prevedelli, J. Stuhler, and G. M. Tino, Atom interferometry gravity-gradiometer for the determination of the newtonian gravitational constant G, Eur. Phys. J. D **40**, 271 (2006).

[15] J. B. Fixler, G. T. Foster, J. M. McGuirk, and M. A. Kasevich, Atom interferometer measurement of the newtonian constant of gravity, Science **315**, 74 (2007).

[16] G. Rosi, F. Sorrentino, L. Cacciapuoti, M. Prevedelli, and G. M. Tino, Precision measurement of the newtonian gravitational constant using cold atoms, Nature **510**, 518 (2014).

[17] S. L. Campbell, R. B. Hutson, G. E. Marti, A. Goban, N. Darkwah Oppong, R. L. McNally, L. Sonderhouse, J. M. Robinson, W. Zhang, B. J. Bloom, and J. Ye, A fermi-degenerate three-dimensional optical lattice clock, Science **358**, 90 (2017).

[18] W. F. McGrew, X. Zhang, R. J. Fasano, S. A. Schäffer, K. Beloy, D. Nicolodi, R. C. Brown, N. Hinkley, G. Milani, M. Schioppo, T. H. Yoon, and A. D. Ludlow, Atomic clock performance enabling geodesy below the centimetre level, Nature **564**, 87 (2018).

[19] Nils Nemitz, Takuya Ohkubo, Masao Takamoto, Ichiro Ushijima, Manoj Das, Noriaki Ohmae, and Hidetoshi Katori, Frequency ratio of Yb and Sr clocks with 5×10^{-17} uncertainty at 150 seconds averaging time, Nat. Photonics **10**, 258 (2016).

[20] Y. Bidel, N. Zahzam, C. Blanchard, A. Bonnin, M. Cadoret, A. Bresson, D. Rouxel, and M. F. Lequentrec-Lalancette, Absolute marine gravimetry with matter-wave interferometry, Nat. Commun. **9**, 627 (2018).

[21] Vincent Ménoret, Pierre Vermeulen, Nicolas Le Moigne, Sylvain Bonvalot, Philippe Bouyer, Arnaud Landragin, and Bruno Desruelle, Gravity measurements below 10^{-9} g with a transportable absolute quantum gravimeter, Sci. Rep. **8**, 12300 (2018).

[22] I. Dutta, D. Savoie, B. Fang, B. Venon, C. L. Garrido Alzar, R. Geiger, and A. Landragin, Continuous Cold-atom Inertial Sensor with 1 nrad/sec Rotation Stability, Phys. Rev. Lett. **116**, 183003 (2016).

[23] Pierrick Cheiney, Lauriane Fouché, Simon Templier, Fabien Napolitano, Baptiste Battelier, Philippe Bouyer, and Brynle Barrett, Navigation-compatible hybrid quantum accelerometer using a Kalman filter, Phys. Rev. Appl **10**, 034030 (2018).

[24] G. J. Dick, in *Proc. Precise Time and Time Interval Meeting*, edited by R. L. Sydnow (US Naval Observatory, Redondo Beach, California, United States, 1987), p. 133.

[25] Audrey Quessada, Richard PKovacich, Irène Courtillot, André Clairon, Giorgio Santarelli, and Pierre Lemonde, The Dick effect for an optical frequency standard, J. Opt. B: Quantum Semiclass. Opt. **5**, S150 (2003).

[26] Masao Takamoto, Tetsushi Takano, and Hidetoshi Katori, Frequency comparison of optical lattice clocks beyond the Dick limit, Nat. Photonics **5**, 288 (2011).

[27] Ali Al-Masoudi, Sören Dörscher, Sebastian Häfner, Uwe Sterr, and Christian Lisdat, Noise and instability of an optical lattice clock, Phys. Rev. A **92**, 063814 (2015).

[28] T. Kessler, C. Hagemann, C. Grebing, T. Legero, U. Sterr, F. Riehle, M. J. Martin, L. Chen, and J. Ye, A sub-40 mhz linewidth laser based on a silicon single-crystal optical cavity, Nat. Photonics **6**, 687 (2012).

[29] Sebastian Häfner, Stephan Falke, Christian Grebing, Stefan Vogt, Thomas Legero, Mikko Merimaa, Christian Lisdat, and Uwe Sterr, 8×10^{-17} fractional laser frequency instability with a long room-temperature cavity, Opt. Lett. **40**, 2112 (2015).

[30] G. W. Biedermann, K. Takase, X. Wu, L. Deslauriers, S. Roy, and M. A. Kasevich, Zero-dead-time Operation of Interleaved Atomic Clocks, Phys. Rev. Lett. **111**, 170802 (2013).

[31] M. Schioppo, R. C. Brown, W. F. McGrew, N. Hinkley, R. J. Fasano, K. Beloy, T. H. Yoon, G. Milani, D. Nicolodi, J. A. Sherman, N. B. Phillips, C. W. Oates, and A. D. Ludlow, Ultrastable optical clock with two cold-atom ensembles, Nat. Photonics **11**, 48 (2016).

[32] R. Kohlhaas, A. Bertoldi, E. Cantin, A. Aspect, A. Landragin, and P. Bouyer, Phase Locking a Clock Oscillator

to a Coherent Atomic Ensemble, Phys. Rev. X **5**, 021011 (2015).
[33] Matthew A. Norcia, Aaron W. Young, William J. Eckner, Eric Oelker, Jun Ye, and Adam M. Kaufman, Seconds-scale coherence in a tweezer-array optical clock, arXiv:1904.10934 (2019).
[34] P. Westergaard, J. Lodewyck, and P. Lemonde, Minimizing the Dick effect in an optical lattice clock, IEEE Trans. Ultrason. Ferroelectr. Freq. Control **57**, 623 (2010).
[35] David W. Keith, Christopher R. Ekstrom, Quentin A. Turchette, and David E. Pritchard, An Interferometer for Atoms, Phys. Rev. Lett. **66**, 2693 (1991).
[36] D. S. Durfee, Y. K. Shaham, and M. A. Kasevich, Long-term Stability of an Area-reversible Atom-interferometer Sagnac Gyroscope, Phys. Rev. Lett. **97**, 240801 (2006).
[37] A. Jallageas, L. Devenoges, M. Petersen, J. Morel, L. G. Bernier, D. Schenker, P. Thomann, and T. Südmeyer, First uncertainty evaluation of the FoCS-2 primary frequency standard, Metrologia **55**, 366 (2018).
[38] Hongbo Xue, Yanying Feng, Shu Chen, Xiaojia Wang, Xueshu Yan, Zhikun Jiang, and Zhaoying Zhou, A continuous cold atomic beam interferometer, J. Appl. Phys. **117**, 094901 (2015).
[39] JingBiao Chen, Active optical clock, Chin. Sci. Bull. **54**, 348 (2009).
[40] D. Meiser, Jun Ye, D. R. Carlson, and M. J. Holland, Prospects for a Millihertz-linewidth Laser, Phys. Rev. Lett. **102**, 163601 (2009).
[41] Justin G. Bohnet, Zilong Chen, Joshua M. Weiner, Dominic Meiser, Murray J. Holland, and James K. Thompson, A steady-state superradiant laser with less than one intracavity photon, Nature **484**, 78 (2012).
[42] Matthew A. Norcia, Matthew N. Winchester, Julia R. K. Cline, and James K. Thompson, Superradiance on the millihertz linewidth strontium clock transition, Sci. Adv. **2**, e1601231 (2016).
[43] Juan A. Muniz, Julia R. K. Cline, Matthew A. Norcia, and James K. Thompson, in *Optical, Opto-Atomic, and Entanglement-Enhanced Precision Metrology*, (SPIE, San Francisco, California, United States, 2019), Vol. 10934.
[44] https://www.iqclock.eu/.
[45] Christopher Jekeli, Navigation error analysis of atom interferometer inertial sensor, Navigation **52**, 1 (2005).
[46] N. P. Robins, P. A. Altin, J. E. Debs, and J. D. Close, Atom lasers: Production, properties and prospects for precision inertial measurement, Phys. Rep. **529**, 265 (2013).
[47] T. Lahaye, J. M. Vogels, K. J. Günter, Z. Wang, J. Dalibard, and D. Guéry-Odelin, Realization of a Magnetically Guided Atomic Beam in the Collisional Regime, Phys. Rev. Lett. **93**, 093003 (2004).
[48] T. Lahaye, Z. Wang, G. Reinaudi, S. P. Rath, J. Dalibard, and D. Guéry-Odelin, Evaporative cooling of a guided rubidium atomic beam, Phys. Rev. A **72**, 033411 (2005).
[49] A. Aghajani-Talesh, M. Falkenau, V. V. Volchkov, L. E. Trafford, T. Pfau, and A. Griesmaier, Laser cooling of a magnetically guided ultracold atom beam, New J. Phys. **12**, 065018 (2010).
[50] Markus Falkenau, Valentin V. Volchkov, Jahn Rührig, Axel Griesmaier, and Tilman Pfau, Continuous Loading of a Conservative Potential Trap from an Atomic Beam, Phys. Rev. Lett. **106**, 163002 (2011).
[51] B. Knuffman, A. V. Steele, and J. J. McClelland, Cold atomic beam ion source for focused ion beam applications, J. Appl. Phys. **114**, 044303 (2013).
[52] Tomoya Akatsuka, Tadahiro Takahashi, and Hidetoshi Katori, Optically guided atom interferometer tuned to magic wavelength, Appl. Phys Express **10**, 112501 (2017).
[53] Liang Hu, Nicola Poli, Leonardo Salvi, and Guglielmo M. Tino, Atom Interferometry with the Sr Optical Clock Transition, Phys. Rev. Lett. **119**, 263601 (2017).
[54] Kamanasish Debnath, Yuan Zhang, and Klaus Mølmer, Lasing in the superradiant crossover regime, Phys. Rev. A **98**, 063837 (2018).
[55] E. W. Hagley, L. Deng, M. Kozuma, J. Wen, K. Helmerson, S. L. Rolston, and W. D. Phillips, A well-collimated quasi-continuous atom laser, Science **283**, 1706 (1999).
[56] W. Guerin, J.-F. Riou, J. P. Gaebler, V. Josse, P. Bouyer, and A. Aspect, Guided Quasicontinuous Atom Laser, Phys. Rev. Lett. **97**, 200402 (2006).
[57] E. Mandonnet, A. Minguzzi, R. Dum, I. Carusotto, Y. Castin, and J. Dalibard, Evaporative cooling of an atomic beam, Eur. Phys. J. D **10**, 9 (2000).
[58] Spencer E. Olson, Georg Raithel, and Andrew J. Christlieb, Pressure-driven evaporative cooling in atom guides, Phys. Rev. A **90**, 043612 (2014).
[59] Shayne Bennetts, Chun-Chia Chen, Benjamin Pasquiou, and Florian Schreck, Steady-state Magneto-optical Trap with 100-fold Improved Phase-space Density, Phys. Rev. Lett. **119**, 223202 (2017).
[60] Wolfgang Ketterle, Kendall B. Davis, Michael A. Joffe, Alex Martin, and David E. Pritchard, High Densities of Cold Atoms in a Dark Spontaneous-force Optical Trap, Phys. Rev. Lett. **70**, 2253 (1993).
[61] J. J. McClelland, A. V. Steele, B. Knuffman, K. A. Twedt, A. Schwarzkopf, and T. M. Wilson, Bright focused ion beam sources based on laser-cooled atoms, Appl. Phys. Rev. **3**, 011302 (2016).
[62] F. Lison, P. Schuh, D. Haubrich, and D. Meschede, High-brilliance Zeeman-slowed cesium atomic beam, Phys. Rev. A **61**, 013405 (1999).
[63] R. D. Glover and T. Bastin, Optical collimation of an atomic beam using a white light molasses, J. Opt. Soc. Am. B **32**, B1 (2015).
[64] Philipp Treutlein, Keng Yeow Chung, and Steven Chu, High-brightness atom source for atomic fountains, Phys. Rev. A **63**, 051401 (2001).
[65] Tangi Miossec, René Barbé, Jean-Claude Keller, and Olivier Gorceix, Pulsed magnetic lenses for producing intense and bright cold atom beams, Opt. Commun. **209**, 349 (2002).
[66] Erling Riis, David S. Weiss, Kathryn A. Moler, and Steven Chu, Atom Funnel for the Production of a Slow, High-density Atomic Beam, Phys. Rev. Lett. **64**, 1658 (1990).
[67] H. Chen and E. Riis, Cold atomic beam from a rubidium funnel, Appl. Phys. B **70**, 665 (2000).
[68] Immanuel Bloch, Theodor W. Hänsch, and Tilman Esslinger, Atom Laser with a cw Output Coupler, Phys. Rev. Lett. **82**, 3008 (1999).
[69] N. P. Robins, C. Figl, S. A. Haine, A. K. Morrison, M. Jeppesen, J. J. Hope, and J. D. Close, Achieving Peak Brightness in an Atom Laser, Phys. Rev. Lett. **96**, 140403 (2006).

[70] William D. Phillips and Harold Metcalf, Laser Deceleration of an Atomic Beam, Phys. Rev. Lett. **48**, 596 (1982).

[71] M. Anderlini, D. Ciampini, D. Cossart, E. Courtade, M. Cristiani, C. Sias, O. Morsch, and E. Arimondo, Model for collisions in ultracold-atom mixtures, Phys. Rev. A **72**, 033408 (2005).

[72] D. Meiser and M. J. Holland, Steady-state superradiance with alkaline-earth-metal atoms, Phys. Rev. A **81**, 033847 (2010).

[73] G. A. Kazakov and T. Schumm, Stability analysis for bad cavity lasers using inhomogeneously broadened spin-1/2 atoms as a gain medium, Phys. Rev. A **95**, 023839 (2017).

[74] Yuan Zhang and Klaus Mølmer, Magnetic field control of optical transmission and narrow linewidth superradiant lasing by strontium atoms, arXiv:1902.06706 (2019).

[75] Stefan A. Schäffer, Mikkel Tang, Martin R. Henriksen, Asbjørn A. Jørgensen, Bjarke T. R. Christensen, and Jan W. Thomsen, Lasing on a narrow transition in a cold thermal strontium ensemble, arXiv:1903.12593 (2019).

[76] Christoph Hotter, David Plankensteiner, Laurin Ostermann, and Helmut Ritsch, Superradiant cooling, trapping, and lasing of dipole-interacting clock atoms, arXiv:1906.01945 (2019).

[77] C. Ates, I. Lesanovsky, C. S. Adams, and K. J. Weatherill, Fast and Quasideterministic Single ion Source from a Dipole-blockaded Atomic Ensemble, Phys. Rev. Lett. **110**, 213003 (2013).

[78] C. Sahin, P. Geppert, A. Müllers, and H. Ott, A high repetition deterministic single ion source, New J. Phys. **19**, 123005 (2017).

[79] Chun-Chia Chen, Shayne Bennetts, Rodrigo González Escudero, Florian Schreck, and Benjamin Pasquiou, Sisyphus optical lattice decelerator, Phys. Rev. A **100**, 023401 (2019).

[80] Spencer E. Olson, Rahul R. Mhaskar, and Georg Raithel, Continuous propagation and energy filtering of a cold atomic beam in a long high-gradient magnetic atom guide, Phys. Rev. A **73**, 033622 (2006).